

Solar Burst Analysis with 3D Loop Models

Joaquim Eduardo Rezende COSTA¹ Paulo José de Aguiar SIMÕES² Tereza Satiko Nishida PINTO^{1,3} and Victor Fedorovich MELNIKOV⁴

¹*Astrophysics Division, National Institute for Space Research, Av. Astronautas, 1758, 12227-010 São José dos Campos, Brazil*

²*SUPA, School of Physics and Astronomy, University of Glasgow, Scotland*

³*Nobeyama Solar Radio Observatory, National Astronomical Observatory of Japan, Minamimaki, Minamisaku, Nagano 384-1305*

⁴*Central Astronomical Observatory at Pulkovo of the Russian Academy of Sciences, Saint-Petersburg 196140, Russia
jercosta@das.inpe.br*

(Received ; accepted)

Abstract

A sample of Nobeyama flares was selected and analyzed using loop model for important flare parameters. The model for the flaring region consists of a three dimensional dipolar magnetic field, and spatial distributions of nonthermal electrons. We constructed a database by calculating the flare microwave emission for a wide range of these parameters. Out of this database with more than 5,000 cases we extracted general flare properties by comparing the observed and calculated microwave spectra. The analysis of NoRP data was mostly based in the center to limb variation of the flare properties with looptop and foot-point electron distributions and for NoRH maps on the resultant distribution of emission. One important aspect of this work is the comparison of the analysis of a flare using an inhomogeneous source model and a simplistic homogeneous source model. Our results show clearly that the homogeneous source hypothesis is not appropriate to describe the possible flare geometry and its use can easily produce misleading results in terms of non-thermal electron density and magnetic field strength. A center darkening of flares was also obtained as a geometrical property of the loop-like sources

Key words: Sun: radio radiation, Sun: flares, Sun: magnetic fields, Sun: atmosphere, catalogs

1. Introduction

Solar flares are associated with magnetic loops or arcades, where accelerated particles move along the field, and can be trapped due to magnetic mirroring or precipitate into the chromosphere, where they produce hard X-rays by bremsstrahlung. The radio/microwave flare emission is produced by electrons moving in the magnetic field due to the gyrosynchrotron mechanism. It has been widely demonstrated that the characteristics of this radiation (spectrum, polarization, spatial distribution) are strongly dependent on the magnetic field strength and geometry, as well as the properties of the non-thermal electrons, such as energy, pitch-angle and spatial distributions (Alissandrakis & Preka-Papadema 1984; Klein & Trotter 1984; Melnikov, Shibasaki & Reznikova 2002; Fleishman & Melnikov 2003; Simões and Costa 2006; Reznikova et al. 2009; Simões & Costa 2010) . High spatial resolution flare observations in microwaves with the Nobeyama Radio Heliograph (NoRH), Very Large Array (VLA) and Owen Valley Solar Array (OVSA) and in X-rays with Yohkoh and Reuven Ramaty High Energy Solar Spectroscopic Imager (RHESSI) have shown a great variety of source morphologies, interpreted as magnetic arcades, interaction between two or more loops, and many others. Nevertheless, it seems that many flares can be associated with a single magnetic loop, i.e. conjugated footpoints connected by a coronal loop (e.g. Melnikov

2006; Tomczak & Ciborski 2007; Tzatzakis, Nindos, & Alissandrakis 2008).

The lack of knowledge on the coronal magnetic field usually leads to simple homogenous source model to analyze the emission, although simple field geometries were proposed to model the observed microwave emission of specific flares (Nindos et al. 2000; Kundu et al. 2001). To describe a spatially varying flare source, it is necessary to define the strength and geometry of the magnetic field, spatial distribution of the non-thermal electrons, and to a lesser importance for microwave emission, the thermal plasma density and temperature, which can be relevant to the free-free absorption and Razin effect. To improve our actual knowledge from the flare homogeneous modeling we constructed a database of models using a three dimensional dipolar loop geometry and searched for the ranges of parameters to describe the observables. The implementation of a dipolar loop geometry is a great improvement from the homogeneous flare model in terms of the description of the flare source.

The motivation of our work was the construction of a models database to be a framework for a joint analyzes of microwave solar flares. We searched for the set of geometrical conditions to a magnetic bottle that reproduce the statistical properties of the spectra observed by the Nobeyama Radio Polarimeter (NoRP) (Nakajima et al. 1985; Torii et al. 1979) and the brightness distribution maps observed by the Nobeyama Radioheliograph

(NoRH) (Nakajima et al. 1994; Takano et al. 1997). The aim of the work was not to construct a new interactive tool for flare analysis, but to present an ensemble of models with emission characteristics similar of those observed flares to infer physical

parameters of flare loops from this set and evaluate the risk of getting misleading results.

Our approach can be considered as a first order approximation of the realistic distribution of parameters. Considering actual understanding of flare emission in microwaves about emission mechanisms, geometry, particle distribution in energy and space and the flare ambient (density and magnetic field), we constructed the template of our model, in a similar fashion to other interesting works of Simões & Costa 2010, Nita et al. 2009; Kuznetsov et al. 2011 and references therein. To analyze the flare properties of our database we calculated more than 5,000 models with a range of parameters capable to reproduce the observed flare characteristics, such as flux densities, spectrum characteristics and source sizes.

2. Heliographic distribution of flares

Figure 1a shows NoRH flare's heliographic coordinates for 600 observed events in all possible latitudes as known from the butterfly diagram of the active regions. It is noticeable the lack of flares observed at disk center (Costa et al. 2010).

The distribution of flares in apparent latitude (i. e., in relation to the visual center) also shows a strong decrease of the flares at the disk center, as shown in the Figure 1b. In this distribution we used the central angle as the position coordinate of the flare. The central angle is defined as the angle between the normal of flare position and the normal to the disk center. This defines 0° and 90° as the disk centre and solar limb, respectively. Although we see flares near the visual equator the center to limb distribution of flares is not homogeneous. Around 80° there is an abrupt decrease in the number of flares, most likely due to imprecision in measuring the position close to the limb or to auto eclipse. Center angles smaller than 20° show a smaller number of flares, i. e., at disk center there is a deficit of events. This result is a strong motivation for this work, as position and geometry of flaring loops may explain these results. There is a strong dependence of the gyrosynchrotron emission with the angle between the magnetic field and the line of sight (θ). If most of the emission comes from the footpoints and legs of the magnetic bottle, at the disk center the angle of the magnetic field, θ , tends to zero and the emission becomes negligible, resulting in the observed effect of missing flares.

3. Model Description

The canonical geometry for a solar flare is a magnetic bottle where the accelerated particles are trapped by magnetic mirroring and emit microwave radiation. The geometry in the numerical model was based on an analytic dipole magnetic loop, which can be placed in any position

observed by NoRH. The magnetic field lines to be populated by thermal plasma and nonthermal electrons are free parameters restricted only by observed source sizes in 17 GHz at NoRH brightness maps. Finally, microwave images are computed in any chosen frequency. Ambient density and temperature were filled using plan-parallel atmospheric model, with distance from the center of the Sun. The non-thermal electron density was filled with distance from the top of the structure and considering the total length of the line.

3.1. Magnetic field model

To define the flaring loop magnetic field we used a dipole magnetic field described by:

$$B = \frac{3(\boldsymbol{\mu}\mathbf{r})\mathbf{r} - r^2\boldsymbol{\mu}}{r^5} \quad (1)$$

where the dipole is in the origin of coordinates, the \mathbf{r} is the position vector of any voxel in space and $\boldsymbol{\mu}$ is the dipole magnetic moment with absolute value calculated from the model condition of a given maximum magnetic field at the loop footpoint (see figure 2). The figure 2 shows a magnetic dipole with a moment μ parallel to the tangent of the solar surface. The dipole is placed below the solar surface at depth d . The maximum magnetic field strength is a free parameter for the lowest level of the loop volume ($B(h)$), where h is the modulus of the position vector \mathbf{h} of the footpoint. The flaring volume is constructed around the central field line with a circular cross-section with radius at the apex of l_r as shown in figure 2. Thus, the geometrical free parameters are the loop height ($H = l_h - d$), feet separation (l_s) and apex radius (l_r). The dipole depth (d) below the surface is calculated from the selected H and l_s which in turn changes the mirror ratio ($B(l_h)/B(h)$). The loop can be placed in any position on the Sun, by defining its latitude and longitude, and with any azimuth angle i. e. the rotation in relation with the solar equator. This geometry is defined inside a $32 \times 32 \times 32$ voxels (volume units) cube. The Z direction points to the observer whatever is the solar position. The viewing angle θ , i. e. the angle between the magnetic field direction at each point and the observer line-of-sight, is calculated from the dipole field lines.

3.2. Spatial distribution of particles

3.2.1. Non-thermal electrons

The description of the distribution functions of the non-thermal electrons in solar flares is still one of the critical unanswered. Several processes such as Coulomb collisions, wave-particle interactions, return currents, magnetic trapping can influence the transport of electrons, and this still is subject of intense investigation. However, a detailed description of such transport processes to evaluate the spatial distribution of electrons is out of the scope of our analysis; moreover, the computing time of these solutions is known to be in a non practical scale for a big number of calculations. To restrict the computing time, we defined empirical functions for the electron distributions in energy and space.

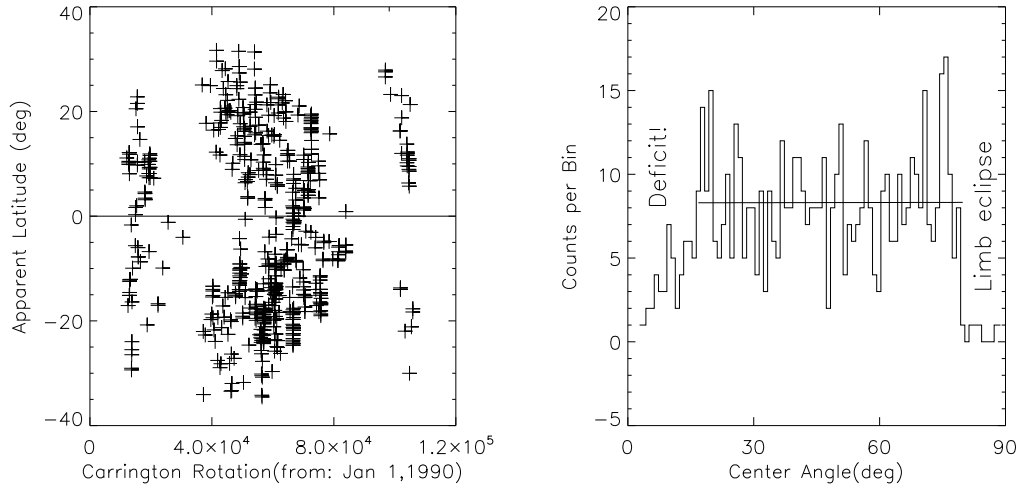


Fig. 1. Left frame: Butterfly diagram with apparent heliographic latitude (without the correction for the tilt of the solar equator to the ecliptic). Right frame: Histogram of center angle for NoRH flares.

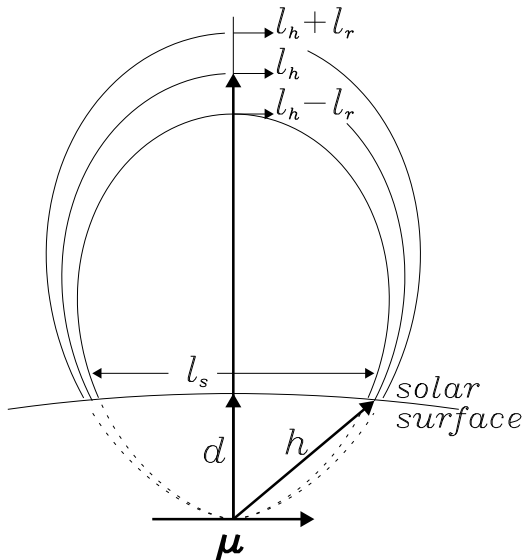


Fig. 2. Magnetic model.

For the energy distribution, we adopted a single power law distribution (with power index δ as a free parameter), in the energy range from 10 keV to 100 MeV, in a isotropic pitch-angle distribution. To define the spatial distribution of the electrons $N(s)$ we used an empirical weighting function parametrized by a constant w as follows:

$$N(s) = N_{el} \frac{(2s^4 + w)e^{-2s^2}}{a + bw} \quad (2)$$

where s is the normalized (unit size for all field lines)

distance along the field line from the loop apex and w is the selection parameter for three distributions: looptop, footpoints or homogeneous concentrations, given by $w = 2.0, 0.05, 0.34$, respectively (see figure 3). The normalized s resulted in uniform distribution along the cross section of the loop. The spatial distribution is symmetrical in relation to the apex. Once the geometrical parameters of the loop were defined, each voxel inside the volume has a field line determined by equation 1 that passes through its center, thus the height l_i of that line can be calculated. If $l_h - l_r < l_i < l_h + l_r$ (Figure 2) the voxel associated with the line is marked as internal to the loop volume. This procedure is repeated for all the voxels inside the volume, determining the discrete loop geometry, with a defined number of voxels, and thus the total volume of the loop. Then, the normalization is numerically computed after applying the equation 2 in each normalized voxel distance s . Parameters a and b normalize the weighting function to maintain the total number of trapped electrons inside the loop volume V_{loop} equal to the user defined non-thermal electron number, i. e. $N_{tot} = N_{el} \times V_{loop}$.

Figure 4 shows one case of magnetic loop centered on the heliographic coordinate N30E85. The axis connecting the two footpoints was rotated by 15° in relation to the solar equator. Figure 4 shows the normalized field line length coordinate (s) (zero is the loop apex and one is the footpoint). The color code indicates the distance of the regions to be filled with the nonthermal electron distributions, which simulate looptop or footpoint concentrations. Figure 4 shows an example of electron number density (N_{el}) distribution, where we used the normalized field line length coordinate (s) (zero is the loop apex and one in the footpoint) to fill the loop according to equation 2 for a footpoint concentration of electrons ($w=0.05$).

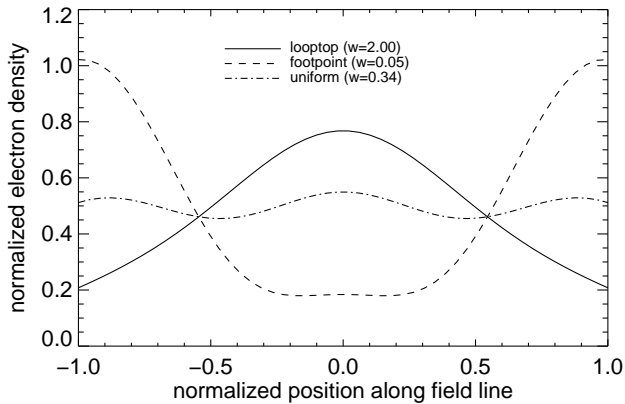


Fig. 3. Weighting function for the three distributions used in the models defined by the equation 2

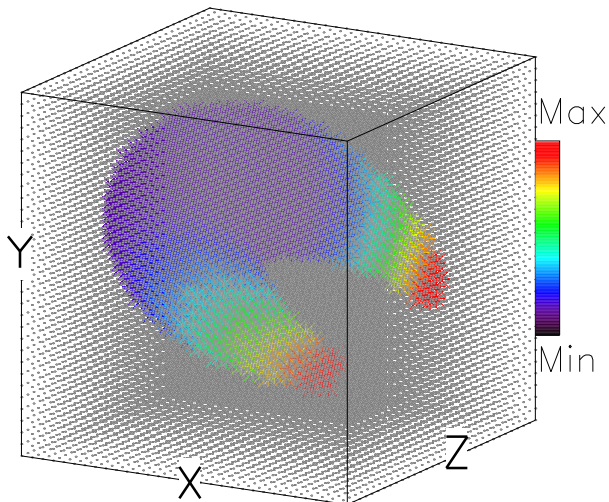


Fig. 4. Apparent loop geometry at N30W85 solar heliographic coordinates. The color coded image shows the electron number density N_{el} , with a footpoint concentration of electrons. Coordinates $[X, Y, Z]$ point to solar East, North, Observer direction, respectively.

3.2.2. Ambient plasma

For the ambient thermal plasma, the temperature was fixed at a high value to minimize the influence of free-free emission typical value during flares at $10^8 K$, that minimizes the free-free contribution; specifically absorption. The density has an exponential decay from 10^{10} cm^{-3} to 10^8 cm^{-3} . With these figures the contributions of bremsstrahlung and the Razin effect in the range of frequency considered in this work were negligible.

3.3. Microwave emission mechanisms

The gyrosynchrotron emission j_ν and self-absorption k_ν coefficients were numerically calculated for the two propagation modes (ordinary and extra-ordinary) using the full formalism (Ramaty 1969). The numerical code was optimized for parallel processing in multi-core processors, and approximations for higher order of the Bessel functions (Wild & Hill 1971) were implemented to improve the computing speed without any significant loss in numerical precision. The effect of Razin suppression is included in our calculations since it is a natural consequence when considering the full gyrosynchrotron formalism, where the production of the radiation is strongly suppressed for frequencies below the Razin frequency $\nu_R = 2\nu_p^2 / (3\nu_B \sin \theta)$ which relates the gyrofrequency ν_B and the plasma frequency ν_p .

The free-free emission and absorption from the thermal plasma are also included in the code, although their effects are not significant for the range of plasma parameters considered here. Also, the Razin effect is not effective in the range of parameters and frequencies here considered. In other words, the construction of this database aimed to reproduce the characteristics of the gyrosynchrotron emission with minimum Razin suppression and free-free contribution.

We noted that for 90% of the Nobeyama sample of flares, the spectral indices in the range of frequencies below the peak frequency (between 3.75 and 9.4 GHz) are smaller than 2.5 (the expected index for gyrosynchrotron emission of non-thermal electrons in homogeneous source in the optically thick part of the spectrum (Dulk 1985)). We emphasize that our model bank is only a first order approximation for the Nobeyama bursts, because of the high number of unknowns that was shortened here for the sake of the decrease the processing time.

The frequencies of the model calculations are 3.7, 9.4, 17, and 34 GHz, selected considering NoRP and NoRH observations. These frequencies allow to study gyrosynchrotron spectrum without contamination from low frequency plasma emission mechanisms (Nita et al. 2004). We did not include 80 GHz as it is not always available in the observational data. The exclusion of such high frequency also speeded up the computing time.

3.4. Solution of the radiative transfer in a 3D source

The ray path in our model is treated as straight lines as in vacuum-like ray trace. This assumption is valid since the refraction indices for the range of frequencies considered here are close to unity for the entire range of source

parameters used in the calculations.

The voxels in our 3D source model were constructed small enough to be considered a homogeneous unit of volume, inside of which all physical variables are uniform. Thus, the analytic solution of the radiative transfer equation can be applied to the voxels at some level ℓ with an input of radiation from the level $\ell - 1$ below. The specific intensity I_ν emerging at each pixel in the XY plane of the source is obtained by:

$$S_{\nu\ell} = \frac{J_{\nu\ell}}{k_{\nu\ell}}(1 - e^{-k_{\nu\ell}\Delta L}) \quad (3)$$

$$I_\nu = \sum_{\ell=2}^n [S_{\nu n} + I_{\nu(\ell-1)}e^{-k_{\nu\ell}\Delta L}] \quad (4)$$

where ℓ is the integration level in the direction of the observer Z , from one (cube bottom) to n (cube top), $J_{\nu\ell}$ is the gyrosynchrotron emission coefficient and $k_{\nu\ell}$ the absorption at frequency ν and level ℓ . The voxel size is ΔL . This procedure is repeated for each frequency, producing emission maps for both modes of propagation. The total flux density maps were obtained by summing the intensity of both modes, then multiplying by the angular size of the pixels. The spatially integrated flux density is easily calculated by summing up all the pixels in each map.

4. Model database

The database was constructed with the 15 variable parameters previously described. In this actual version the selected frequencies were [3.75, 9.4, 17.0, 35.0] GHz, the number of voxels is $32 \times 32 \times 32$, $l_r = 0.007R_\odot$ (where R_\odot is the solar radius), $l_s = 0.02R_\odot$, $H = 0.007R_\odot$, ambient density exponentially decaying with height from $10^{10} - 10^8 \text{cm}^{-3}$, energy range of the power law distribution of nonthermal electrons from 10keV to 100MeV , homogeneous pitch angle distribution and constant ambient temperature at 10^8K . The w constant [0.05, 0.34, 2.] in equation 2 was homogeneously distributed among these three values and the loop azimuth was also equally distributed among $[-60^\circ, -15^\circ, 15^\circ, 60^\circ]$. The loop heliographic position was randomly selected from about 600 positions of flares observed by NoRH. The nonthermal electron number density N_{el} , the power law index of the energy distribution δ and the magnetic field at the footpoint B_{foot} were varied in the ranges shown in table 1. The ranges of parameters were dynamically chosen to reflect the range of flux densities observed by NoRP. The total volume was kept constant as a decision to decrease the parameters' space but also considering results of the NoRH flares at 17 GHz. The actual version of the database has 5,000 computed models and size of 10 GB.

5. Some results

A snapshot from a model can be seen in the figure 5. The Sun is shown at the upper left with the loop over-plotted (the size ten times enlarged for better visualization). Four images of calculated brightness are shown on

Table 1. Range of parameters

Parameter	Minimum	Maximum
B_{foot} (G)	1200	1800
N_{el} (cm^{-3})	10^6	2.5×10^7
δ	1.8	2.4

the upper part. The scale of the images are in arcsec from the Sun center. The integrated flux density for these images are plotted as asterisks on the spectrum at left of the figure. The over-plotted continuum line is the spectrum for a homogeneous source for the parameters shown on the figure. These parameters were calculated from our data cubes to be representative (effective numbers) of our inhomogeneous model. They were calculated using the image with the highest flux density (in this case 17 GHz) with the brightness being the weighting function for all spatially varying parameters.

The source size was calculated to give the same peak flux density of the inhomogeneous model. The result clearly shows that both spectra differs from each other. Based on this difference we may say that even the best representation of our inhomogeneous source by the calculated effective values in a homogeneous approach fails to reproduce the observed spectrum. The figure also shows the distribution of all voxels of magnetic field inside the loop, viewing angle, nonthermal electron number density and ambient density. One thing that strongly support the use of 3D modeling is the viewing angle that dances over the distribution plot under azimuth rotation or changes in heliographic coordinates when maintaining all the rest equal. As the gyrosynchrotron emission strongly depends on viewing angle, the spectra changes accordingly.

5.1. Flux dependencies on the central angle and source size

Although the model bank was constructed only over observed positions for the sake of usability of the models with observations and limitation of the processing time, we observed a general tendency of lower fluxes in the disk center. To obtain a homogeneous distribution of models in center angle we distribute the models in steps of 5° . Out of this distribution we observed 84 models in the first channel (center angle from 0 to 5°) that was calculated over seven observed positions for different flare parameters. Extracting 84 models from each other channel of the distribution randomly selected we averaged the calculated flux densities over the distribution for each frequency of observation. We repeated the process 100 times with different random sequences to average the fluxes in each channel. The result is shown in the figure 6. The decrease in flux of the optically thin emission is clear. The averages of the flux density of our model bank are higher than the averages of observed fluxes, but the shown trend result in negligible fluxes for faint flares yielding to a decrement in the registered flares in any case. We also observe that footpoint concentrations show higher flux dependences in center angle, as expected from the gyrosynchrotron de-

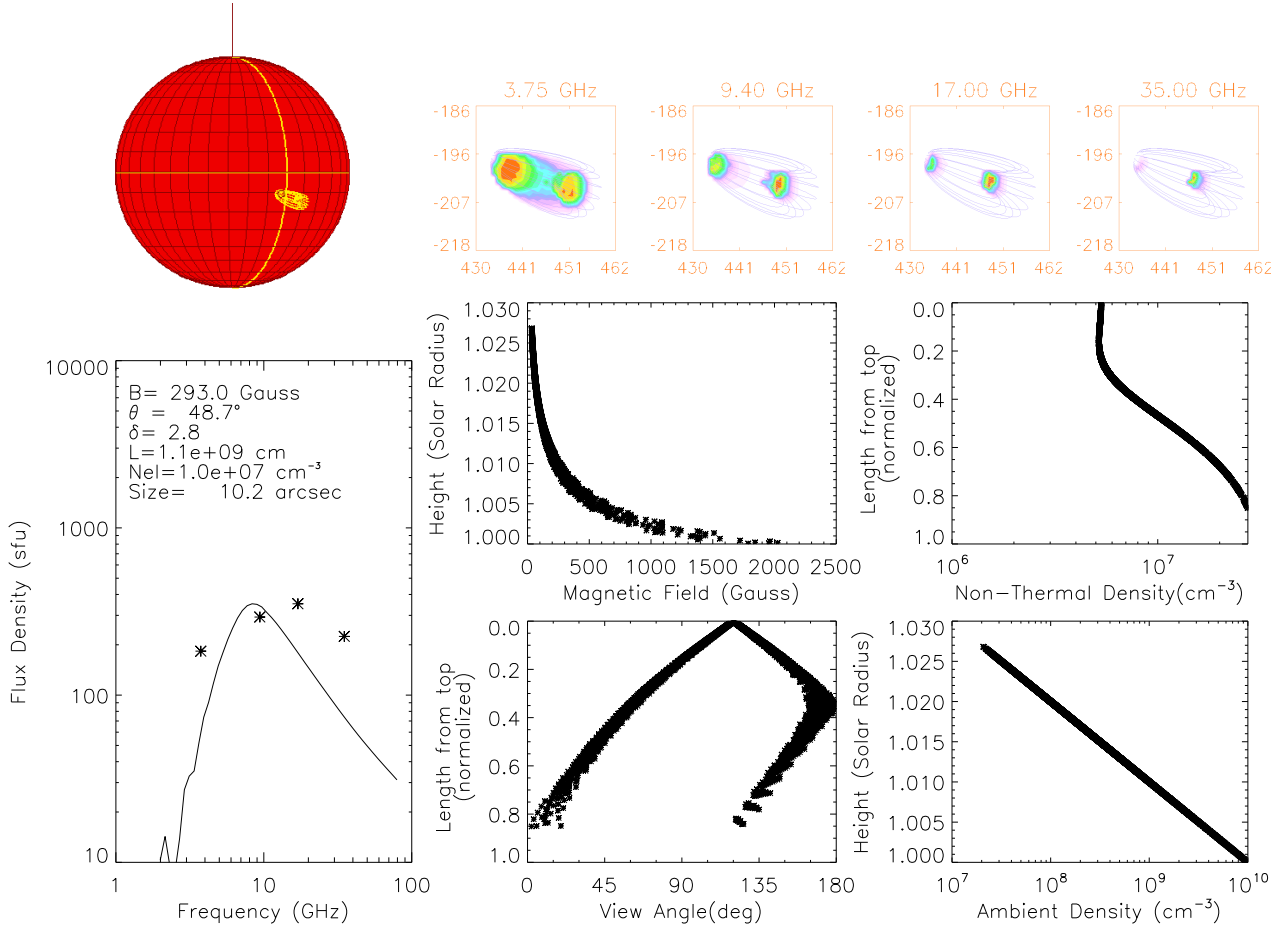


Fig. 5. Model result. Example of one element of the data bank.

pendence on viewing angle.

In the figure 7 we see the effective diameter for different frequencies and flux distribution. We can see that it covers the variation of 17 GHz fluxes but not the size. The flux variation for the four frequencies shown matches the observed range by NoRP. In red diamonds we see 17 GHz from the images with 0.5 arcsec resolution and the points after a convolution by a gaussian beam with 15 arcsec. It is clear that our data bank with fixed loop size fails to represent the observed sizes of 17 GHz (asterisks). We still have to enlarge our loops to account for the bigger sources observed. Also, the dependence of observed fluxes at 17 GHz on size (7) is a characteristic that was not clearly reproduced by our model bank.

5.2. Comparing results

A comparison of the homogeneous source approach with the actual source characteristics of the emission showed important insights. The figure 8 shows a comparison between the effective parameters that describe our data cubes and parameters inferred by a least square fit of a homogeneous source spectrum in the calculated spectrum. We selected from our model bank 909 spectra with peak

frequency (ν_{peak}) lower than 10 GHz. We limited the sample to maintain the 17/34 GHz emission in the optically thin regime to infer the spectral index δ from Dulk's law between radiation spectral index and the electron spectral index (Dulk 1985).

We used a genetic algorithm (Charbonneau 1995) to fit homogeneous spectra on the inhomogeneous spectra data calculated in our data bank. We implemented the genetic algorithm as a robust method to search for the region in the global parameter space associated with the maximum of a figure of merit related to the goodness of the fitting. The goodness of fitting is measured by the maximum of $1/\chi^2$. χ^2 is the summation of squared differences between the observed and calculated flux densities. Some examples of the fitting are shown in figure 9 for three different flares at peak time.

As a homogeneous source model we used a gyrosynchrotron code with four fixed parameters: homogeneous pitch angle distribution, range of energy from 10 keV to 100 MeV, ambient density equal 10^9 cm^{-3} and ambient temperature of 10^8 K , and six variable parameters: electron spectral index δ , nonthermal electron density N_{el} , viewing angle θ , magnetic field B, area and depth. The

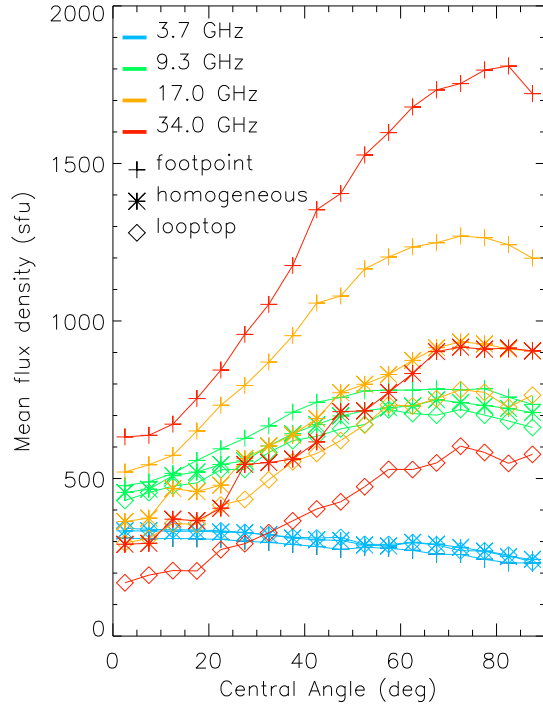


Fig. 6. Averaged flux densities of the model bank versus center angle.

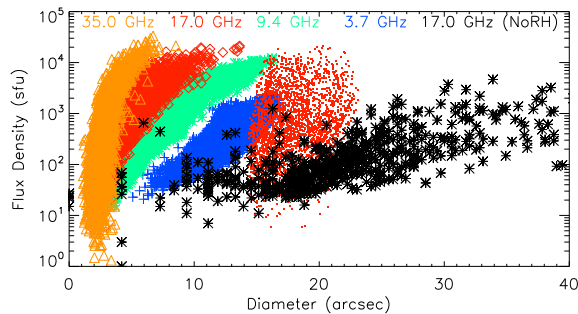


Fig. 7. Integrated flux density versus effective diameter of the emitting area. The red points are the effective diameter for 17 GHz (red diamonds) after convolution with a Gaussian beam of 15 arcsec

population of spectra calculated by the genetic algorithm for each fit had 2100 members and the best fit was then extracted from the minimum χ^2 .

The result can be seen in the figure 8. The X-axes contain the effective parameters that represents the data cubes and Y-axes the inferred parameters from homogeneous approach. The spectral index δ is roughly similar the index used but the rest differs by orders of magnitude. Some of them are overestimated and some are underestimated.

5.3. Some observations

To show the roughly estimation of the characteristics of our data bank we got two flares observed by Nobeyama (NoRP and NoRH) and selected from the data bank the best model to represent both flares by the spectrum and brightness distribution. The number of models calculated is still very modest but the result is quite promising.

Figure 10 shows the December 28, 1999 at 00:43 UT flare with the contour plot of the 17/34 GHz observations over-plotted on the magnetogram observed by MDI on board of SOHO satellite in the part **a** of the figure. Looking inside our data bank we find the best fit model to the spectrum and image of the observed flare as is shown in parts **c** and **d**. In part **c** of the figure some magnetic field lines are plotted. The field lines were extrapolated solving the force free field equation with linear solutions. The $\alpha = 0.04 \text{ Mm}^{-1}$ current parameter was selected to match the orientation of the center line of the loop model. The extrapolated line is $1.7 \times 10^9 \text{ cm}$ long and is roughly equal the length of the loop central line with $2 \times 10^9 \text{ cm}$. The magnetic field at the foot point of this extrapolated line is 1156 Gauss and the maximum magnetic field of the model loop is 1366 Gauss.

Figure 11 shows another observed burst in February 15, 2011 at 01:46 UT. The shown magnetogram is an observation of HMI on board of SDO satellite. The extrapolated field lines in this case is $6.5 \times 10^9 \text{ cm}$ long and the model loop length is $2 \times 10^9 \text{ cm}$. The footpoint magnetic field of the line is 1341 Gauss and the footpoint magnetic field at the loop model is 1518 Gauss.

6. Discussion and conclusions

The missing flares of the Nobeyama sample at the Sun center are likely to flux densities below the instrument sensitivity of the less intense flares that are missed. This is clearly due to the flux density dependence on the viewing angle (as shown in our figure 6). Thus, the geometry of the source may play an important role in the emission as was reviewed here. One important aspect of this is the comparison of the analysis of a flare that was produced inside an inhomogeneous environment and analyzed latter as a simplistic homogeneous source (as shown in the subsection 5.2). Our intent was not to show different methods of homogeneous flare analyzes based in the spectrum fit but to use one method and evaluate the risk of getting misleading results. The genetic algorithm was chosen to be independent of initial guesses and for being robust to

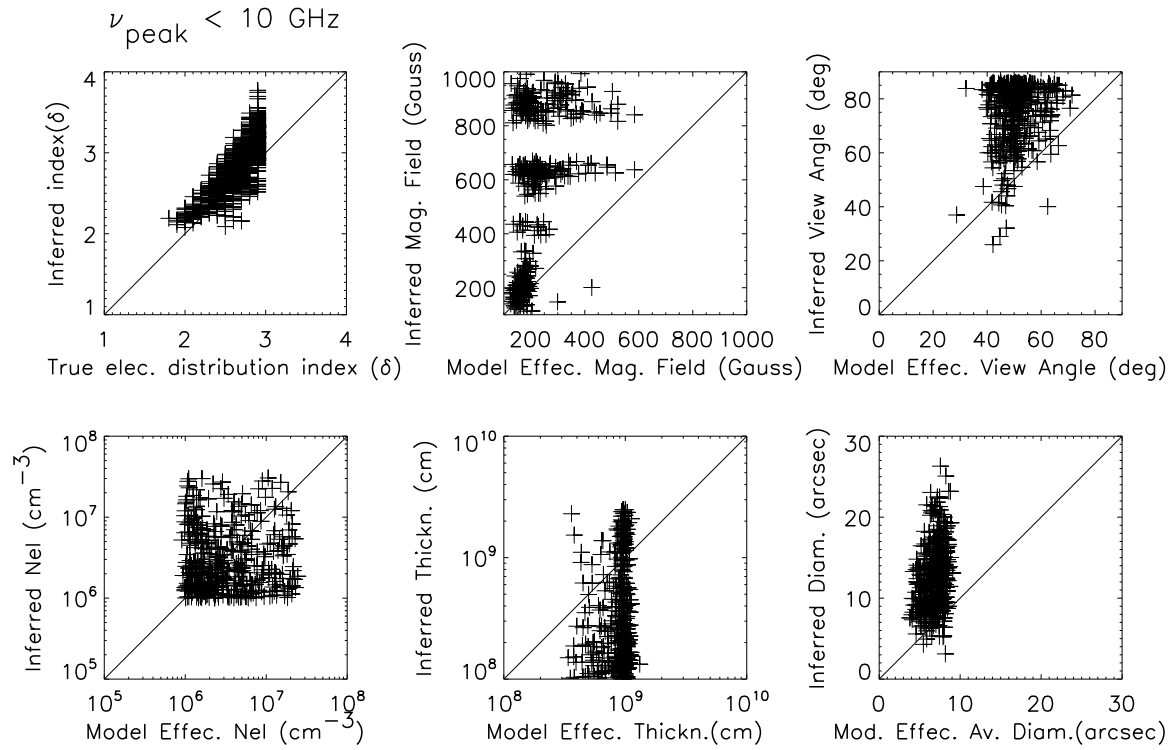


Fig. 8. Comparison between homogeneous and inhomogeneous modeling.

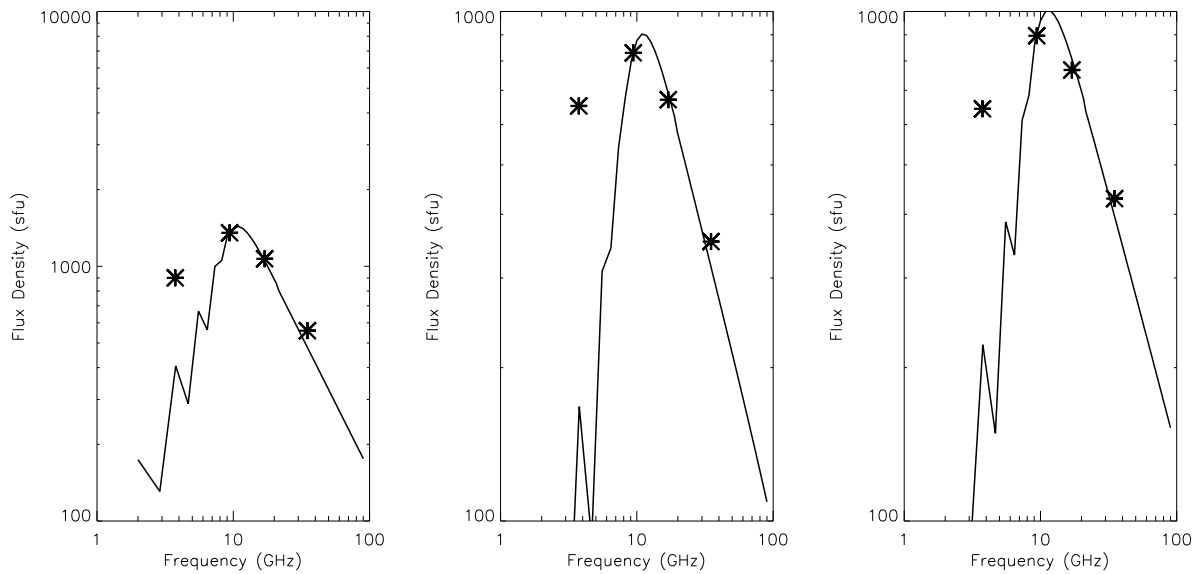


Fig. 9. Spectra fitting of homogeneous source in inhomogeneous data source.

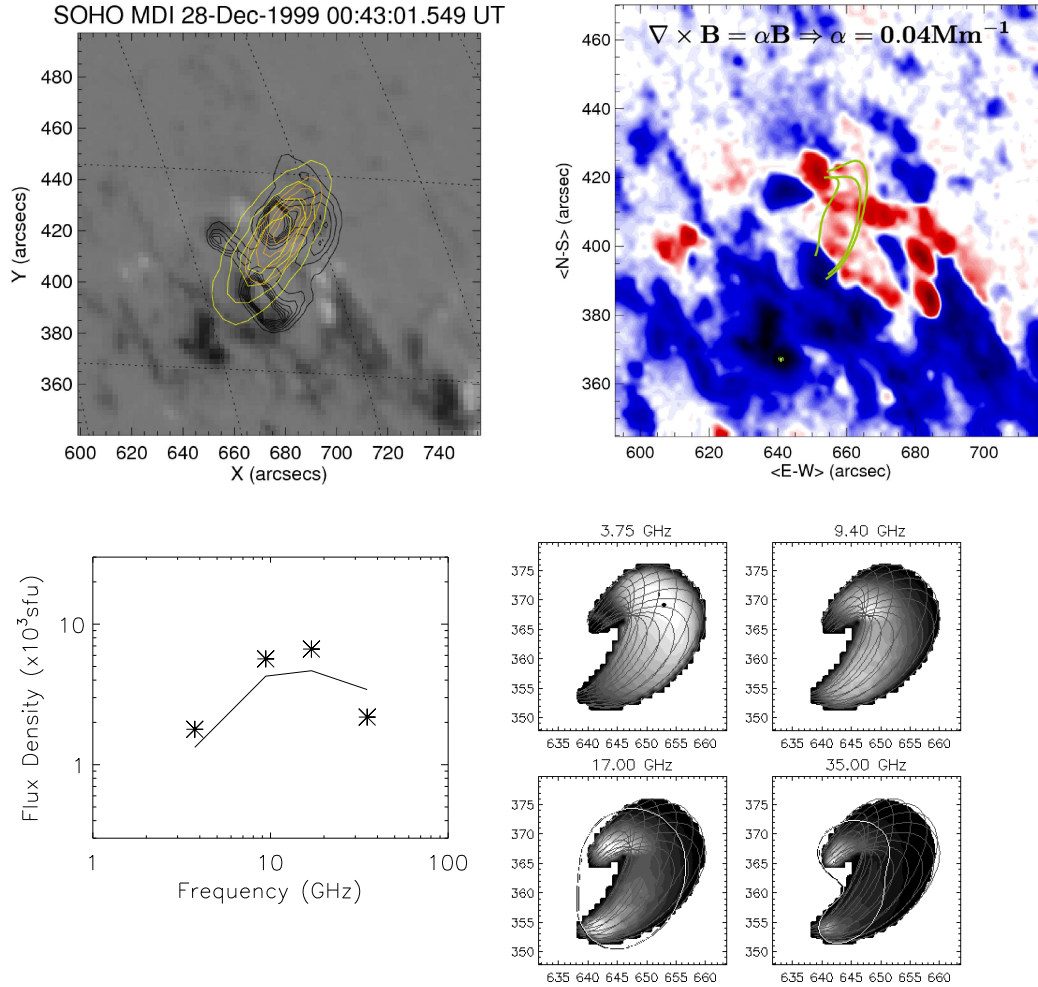


Fig. 10. Nobeyama flare 19991228_0043. Part **a** shows the SDO magnetogram with the contours of 17 GHz in green and 34 GHz in yellow over-plotted. In **b** is the magnetogram with some extrapolated linear force free field lines. In **c** is the observed spectrum (asterisks) and the model spectrum (line). In **d** is the model brightness distribution with field lines over-plotted and contours in 17 and 34 GHz after gaussian beam convolution (15 and 8 arcsec, respectively). The SOHO is a project of international cooperation between ESA and NASA.

search for a global maximum for the figure of merit in the parameters space. It is clear that the homogeneous source hypothesis is not appropriate to the possible flare geometry.

The data bank of the models increases our capacity of flare analysis with a 3D loop model and understanding of flare properties. We mention, for example, that in the figure 7 the roughly correlation of the observed flux density with source diameter at 17GHz is not obtained by the models with fixed loop size. Even if the model bank includes larger loops this may result in a broad range of flux versus diameter instead of a correlation. This property will be analyzed in a future tuning of the model bank. The first analysis of NoRP and NORH flares is encouraging as shown by figures 10 and 11. These analyzes were done by searching inside spectra bank given the flare heliographic position. This is an IDL routine that searches inside a structured variable with all parameters of the models. With the best fits of the spectra one may se-

lect the model with best the azimuth for the Nobeyama Radioheliograph observed map.

Final refinements can be achieved in the future work calculating new models using different azimuth and loop size or any other flare parameters such as the plasma density and magnetic field strength. Taking into account the Razin effect may be important for the flare analysis. It is known that Razin suppression plays significant role at lower microwave frequencies, $\nu < 10$ GHz, for a large percentage of flares ($> 50\%$) observed with the spectrometer of Owens Valley Solar Array (Melnikov, Gary & Nita 2008). Strong Razin suppression was also detected with NoRH even at frequency 17 GHz but only for some flares (Melnikov et al. 2005; Kuznetsov & Melnikov 2012). It means that the higher ratios n_0/B may happen in real solar flaring loops than it is taken in our model.

For the two flares shown in figures 10 and 11 no refinement was made, thus they reflect properties of the actual model bank. They were chosen because one of us

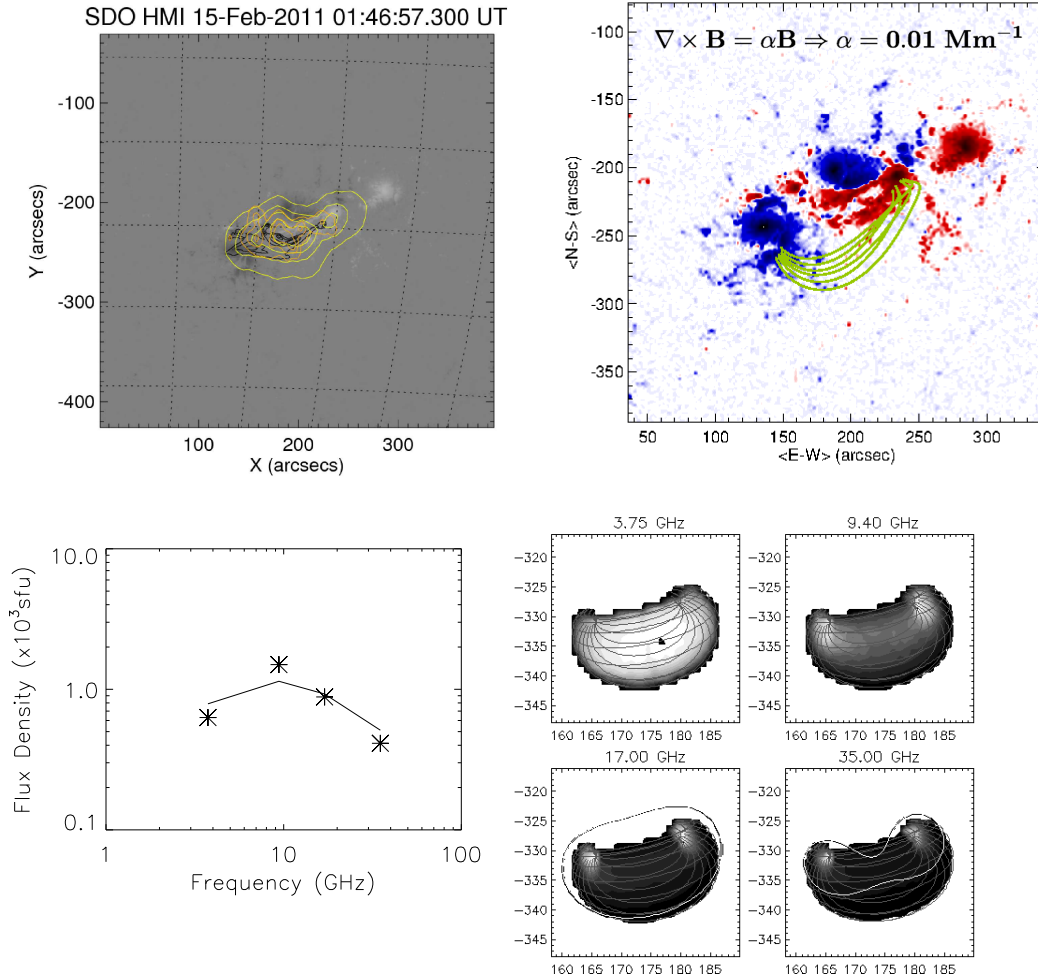


Fig. 11. Nobeyama flare 20110215_0154. Same as figure 10. The SDO images are a courtesy of NASA/SDO and the AIA, EVE, and HMI science teams.

(T.S.N.Pinto) is analyzing the possibility to use force free extrapolation to render the loop volume for another publication.

7. Acknowledgements

We would like to thank the Nobeyama Radioheliograph, which is operated by the NAOJ/Nobeyama Solar Radio Observatory. For two of us (P.J.A. and V.F.M.), this research was partly supported by the Maria Curie Exchange Program grant MC FP7-PEOPLE-2011-IRSES-295272. Also, P.J.A. gratefully acknowledges financial support by the European Commission through HESPE (FP7-SPACE-2010-263086). TSNP visited NSRO with support from the Japanese International Cooperation Agency (JICA)

References

- Alissandrakis, C. E. & Preka-Papadema, P., 1984, *A&A*, 139, 507
- Aschwanden, M. J. and Benz, A. O., 1997, *ApJ*, 480, 825
- Charbonneau, P., 1995, *ApJS*, 101, 309
- Costa, J. E. R., Simões, P. J. A., Giménez de Castro, C.G., *CESRA Workshop on: Energy storage and release through the solar activity cycle - models meet radio observations*, La Roche-en-Ardenne, Belgium, 15 –19 June 2010.
- Dulk, G. A., 1985, *ARA&A*, 23, 169
- Fleishman, G. D., & Melnikov, V. F. 2003, *ApJ*, 584, 1071
- Hamilton, R. J, Lu, E. T. & Petrosian, V., 1990, *ApJ*, 354, 726
- Hanaoka, Y., 1997, *Sol. Phys.*, 173, 319
- Klein, K.-L. and Trotter, G., 1984, *A&A*, 141, 67
- Kundu, M. R., Nindos, A., White, S. M. & Grechnev, V. V., 2001, *ApJ*, 557, 880
- Kuznetsov, A. A, Nita, G. M. & Fleishman, G. D., 2011, *ApJ*, 742, 87
- Kuznetsov S. A. & Melnikov V. F., 2012, *Geomagnetism and Aeronomy*, 52, 883
- Melnikov, V. F., Shibasaki, K., & Reznikova, V. E. 2002, *ApJ*, 580, L185
- Melnikov V. F. , Reznikova V. E., Shibasaki K., Nakariakov V. M., 2005, *Astron. Astrophys.* 439, 727
- Melnikov, V. F. 2006, in *Solar Physics with the Nobeyama Radioheliograph*, NSRO Rep. 1, ed. K. Shibasaki (Nobeyama, Nagano: NSRO), 11
- Melnikov, V. F., Gary, D. E., & Nita, G. M. 2008, *Sol. Phys.*,

- 253, 43
- Nakajima, H., Sekiguchi, H., Sawa, M., Kai, K. & Kawashima, S. 1985, PASJ, 37, 163
- Nakajima, H. and Nishio, M. and Enome, S. and Shibasaki, K. and Takano, T. and Hanaoka, Y. and Torii, C. and Sekiguchi, H. and Bushimata, T. and Kawashima, S. and Shinohara, N. and Irimajiri, Y. and Koshiishi, H. and Kosugi, T. and Shiomi, Y. and Sawa, M. and Kai, K. 1994, Proc. of the IEEE, 82, 705
- Nindos A., White, S. M., Kundu, M. R. & Gary, D. E., 2000, ApJ, 533, 1053
- Nita, G. M., Gary, D. E., & Lee, J., ApJ, 2004, 605, 528
- Nita, G. M., Fleishman, G. D. & Gary, D. E., 2009, in AAS/Solar Physics Division Meeting #40, 15.24
- Ramaty, R., 1969, ApJ, 158, 753
- Reznikova, V. E., Melnikov, V. F., Shibasaki, K., Gorbikov, S. P., Pyatakov, N. P., Myagkova, I., & Ji, H. 2009, ApJ, 297, 735
- Simões, P. J. A. & Costa, J. E. R. 2006, A&A, 453, 729
- _____, 2010, Sol. Phys., 266, 109
- Takano, T. and Nakajima, H. and Enome, S. and Shibasaki, K. and Nishio, M. and Hanaoka, Y. and Shiomi, Y. and Sekiguchi, H. and Kawashima, S. and Bushimata, T. and Shinohara, N. and Torii, C. and Fujiki, K. and Irimajiri, Y. 1997, Coronal Physics from Radio and Space Observations, Lect. Notes Phys., (Berlin: Springer-Verlag), 183
- Tomczak, M. & Ciborski, T., 2007, A&A, 461, 315
- Torii, C., Tsukiji, Y., Kobayashi, S., Yoshimi, N., Tanaka, H. & Enome, S. 1979, *Proceedings of the Research Institute of Atmospheric Physics, Nagoya University*, Nagoya University, 26, 129
- Tzatzakis, V., Nindos, A. & Alissandrakis, C. E., 2008, Sol. Phys., 253, 79
- Wild, J. P. & Hill, E. R., 1971, Australian Journal of Physics, 24, 43